INSTITUTE OF PHYSICS PUBLISHING JOURNAL OF MICROMECHANICS AND MICROENGINEERING

J. Micromech. Microeng. **16** (2006) 1258–1266 doi:10.1088/0960-1317/16/7/020

Modeling and performance of two types of piston-like out-of-plane motion micromechanical structures

Si-Hyung Lim, Roberto Horowitz and Arunava Majumdar

Department of Mechanical Engineering, University of California, Berkeley, CA 94720, USA

E-mail: majumdar@me.berkeley.edu

Received 11 February 2006, in final form 13 February 2006
Published 16 May 2006
Online at stacks.iop.org/JMM/16/1258

Abstract
We have modeled and analyzed the performance of two types of piston-like out-of-plane motion micromechanical structures: a conventional microstructure, which has a single bimorph region, and a flip-over-bimaterial (FOB) microstructure, which has two bimorph regions respectively located on the top and bottom sides of the structure. For both structures, simple analytical expressions of their end-point deflections have been established to facilitate parametric studies in sensor or actuator designs. These structures can be used in several applications such as temperature and chemical sensors, or as actuators for micromirrors. The derived analytical deflection predictions are in good agreement with those made using finite element (FE) models. For a micro-opto-mechanical sensor using interconnected FOB microstructures, these analytical and FE predictions agree with the experimental results within about 25%. Discrepancies can be attributed to uncertainties in the material properties of the specimen being tested. Both the analytically derived deflection expressions and the FE models predict that the FOB microstructures are capable of achieving up to two times higher deflection than conventional microstructures that have a single bimorph region. When compared to a cantilever design, a sensor design having interconnected FOB structures has a higher signal-to-noise ratio for the same device footprint. The analytical modeling and performance analysis presented in this paper can be useful to predict the device performance as well as optimize design parameters.

(Some figures in this article are in colour only in the electronic version)

1. Introduction

Bimorph microstructures have been widely used in physical and bio-chemical sensors [1–7] and actuators [8–12]. Depending on their design and fabrication, these structures deform due to temperature changes, piezoelectric effects, chemical absorption or surface stress induced by molecular interaction. When used to monitor temperature variations [2] or actively move the structures [9, 10, 12], bimorph structures deflect as a result of the thermal expansion mismatch that exists between two different thin film layers. Bimorph microstructures can also deflect by applying a voltage to piezoelectric materials [8, 11]. When used as chemical sensors, analytes may be absorbed by a sensing coating material, which in turn swells and induces strains that cause the microstructure to deform [5]. Finally, surface stress changes due to molecular interaction may also cause these microstructures to deform [1, 3, 4, 6].

Depending on the boundary conditions imposed by their design, bimorph microstructures may experience either an angular cantilever-like deflection or a piston-like out-of-plane motion under the effect of thermal, electrical, chemical or molecular stimuli. When the structures are under a fixed-free boundary condition, bimorph microstructures tend to behave as cantilevers and experience an angular deflection. However, as shown in figure 1, the middle moving part can experience a

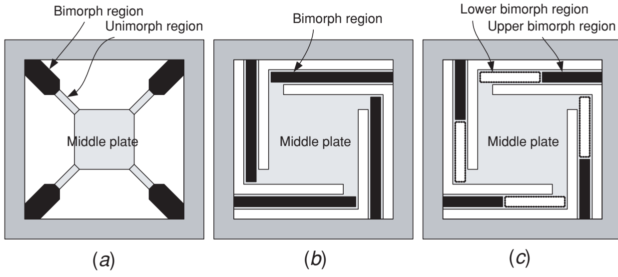

Figure 1. Various piston-like out-of-plane motion configurations. For electrical and thermal stimuli, the middle plates have a piston-like out-of-plane motion due to the deformation of four symmetric microstructural legs. (*a*) Each leg has a bimorph region and a unimorph region [10]. (*b*) Each leg has a bimorph region only [11, 12]. (*c*) Each leg has an upper bimorph region and a lower bimorph region [7].

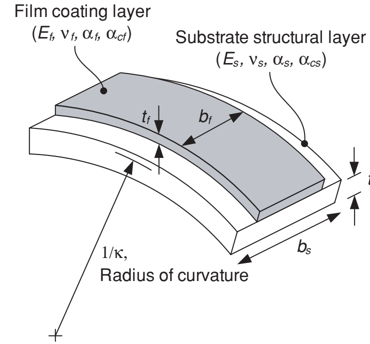

Figure 2. A bimorph model showing material properties and geometrical parameters. The bimorph structure can have structural deformation for various stimuli such as temperature change, the piezoelectric effect, chemical absorption and molecular interaction. E_i, ν_i, α_i and α_{ci} ($i = f$ or s) are the Young's modulus, Poisson's ratio, thermal expansion coefficient and volume expansion coefficient of the film coating layer or substrate structural layer, respectively.

piston-like out-of-plane motion due to the combined action of symmetric bimorph legs under fixed-guided boundary conditions. In order to predict the performance of these devices and to be able to perform parameter optimization searches in the initial stage of their design, it is very important that simple analytical models be derived for their end-point deflection or motion. The deflection model for a cantilever structure has been developed and widely used in many applications [8, 13, 14]. However, a simple model predicting the piston-like out-of-plane motion of microstructures has not been thoroughly studied yet.

Young and Budynas [15] suggested a vertical deflection model for a bimorph structure under fixed-guided boundary conditions. However, this model does not consider the differences in flexural rigidity between the unimorph and bimorph regions. Tuantranont *et al* [10] proposed a micromirror actuator design with a piston-like out-of-plane motion that has four symmetric legs, as shown in figure 1(*a*), with each leg having a bimorph region and a unimorph region, and derived an expression for the vertical deflection of this structure using a nodal displacement method. They derived a vertical deflection model using a nodal displacement method. However, the derived model did not consider the bending moment at the guided boundary, which is necessary to achieve the moment balance of the overall flexure segment. Yee *et al* [11] and Yang *et al* [12] demonstrated the operation of a micromirror using piezoelectric and electro-thermal methods, respectively. However, in both these designs the microstructural legs were completely covered with either piezoelectric (Yee *et al* [11]) or oxide thin films (Yang *et al* [12]), as shown in figure 1(*b*). As a consequence, both these designs were only able to attain a relatively small middle plate deflection, even with the use of long structural legs. For these types of structures, the piston-like out-of-plane motion of the middle plate is greatly affected by the flexibility of the joints that connect it to the structural legs. In the device depicted in figure 1(*b*), each of the four bimorph structural legs is fixed at one end by the substrate and guided at the other end by the middle plate. This fixed-guided boundary condition is different from the fixed-free boundary condition of a simple bimorph cantilever structure, and it severely constrains the motion of the middle plate. Therefore, a different structural leg design must be used to increase the motion of the middle plate, in order to enhance the performance of these devices.

In our previous work, we proposed a novel flip-over-bimaterial (FOB) microstructure design, as shown in figure 1(*c*), to increase sensor sensitivity. The concept was demonstrated with the fabrication and testing of a micro-opto-mechanical sensor array, where each pixel exhibits a piston-like out-of-plane motion [7]. The structural layer of each leg in the FOB structure is coated by two films at different locations. One-half of the structural layer is coated on the top side by a film, while the other half is coated on the bottom side, as depicted in figure 1(*c*). It was also demonstrated that the FOB structure exhibits a higher sensitivity than a conventional microstructure that has only a single bimorph region. However, analytical models for predicting the end-point displacement, sensitivity and signal-to-noise ratio of FOB structures were not derived.

In this paper, we discuss the modeling and performance of two types of bimorph micromechanical structures that exhibit a piston-like out-of-plane motion: microstructures with structural legs that have a single bimorph region and microstructures with FOB structural legs that have two bimorph regions. Simple analytical expressions for predicting the end-point deflection of these devices are derived, which can be used in parametric studies, to facilitate sensor and actuator designs based on these structures. These analytical expressions are compared with finite element (FE) models and both are subsequently used to analyze the sensitivity and signal-to-noise ratio of a sensor design based on these structures.

2. Analytical modeling

2.1. Curvature of the bimorph microstructure

Consider the bimorph structure depicted in figure 2 having a structural layer with biaxial modulus M_s, thickness t_s and width b_s, coated on the top by a film layer of biaxial modulus M_f, thickness t_f and width b_f. Its equivalent flexural rigidity

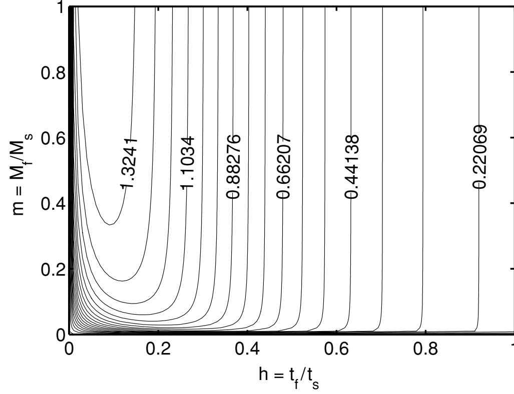

Figure 3. Contour plot of $\kappa t_s/\epsilon_m$ for various thickness ratios $h = t_f/t_s$ and biaxial modulus ratios $m = M_f/M_s$ ($w = 1$).

Table 1. Mismatch strain in various operation mechanisms. These mismatch strains generate the structural deformation of the bimorph structure.

Type	Sources
Thermal expansion mismatch strain ϵ_m^t	Temperature change ΔT
Piezoelectric mismatch strain ϵ_m^p	Electrical voltage input ΔV
Chemical absorption mismatch strain ϵ_m^c	Chemical concentration ΔC
Molecular interaction mismatch strain ϵ_m^s	Surface stress change $\Delta\sigma$

can be calculated using the transformed section method [15]:

$$EI = M_s b_s t_s{}^3 \left[\frac{1 + whm(4 + 6h + 4h^2) + w^2h^4m^2}{12(1 + whm)} \right], \quad (1)$$

where $w \triangleq b_f/b_s$, $h \triangleq t_f/t_s$ and $m \triangleq M_f/M_s$. Also, the curvature of the bimorph structure κ can be calculated by the principle of virtual work method [16]:

$$\kappa = \frac{6w}{t_s} \left[\frac{mh(1 + h)}{1 + wmh(4 + 6h + 4h^2) + h^4w^2m^2} \right] \cdot \epsilon_m, \quad (2)$$

where ϵ_m is a mismatch strain, which arises from several sources (table 1), between the substrate structural layer and the film coating layer. Figure 3 shows the contour plot of the curvature. Each data value corresponds to a nondimensional parameter $\kappa t_s/\epsilon_m$. From this plot, the region of lower thickness ratio ($h < 0.15$) and higher biaxial modulus ratio ($m > 0.35$) gives its higher value.

For a temperature change ΔT, the mismatch strain between the film and substrate can be expressed as

$$\epsilon_m{}^t = (\alpha_f - \alpha_s) \cdot \Delta T, \quad (3)$$

where α_f and α_s are thermal expansion coefficients of the film coating and substrate structural layers, respectively. For an electrical input voltage ΔV to a piezoelectric film coating layer, the mismatch strain can be expressed as

$$\epsilon_m{}^p = d_{31} \frac{\Delta V}{t_f}, \quad (4)$$

where d_{31} is the transverse-piezoelectric-coupling coefficient. Also, for a chemical concentration change ΔC, the mismatch strain can be expressed as [5]

$$\epsilon_m{}^c = (\alpha_{cf} - \alpha_{cs}) \cdot \Delta C, \quad (5)$$

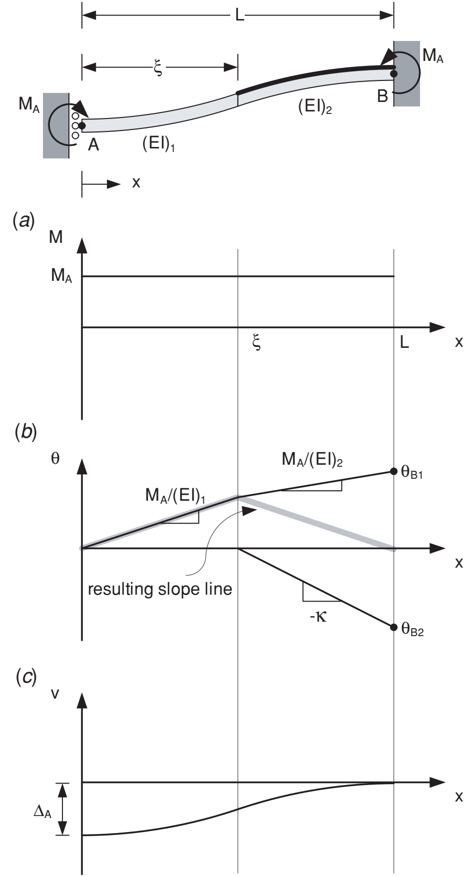

Figure 4. Moment, slope and deflection diagrams of a conventional microstructure having a single bimorph region under a fixed-guided boundary condition.

where α_{cf} and α_{cs} are volume expansion coefficients of the film coating and substrate structural layers, respectively. On the other hand, for a surface stress change $\Delta\sigma$, the mismatch strain is

$$\epsilon_m{}^s = \frac{\Delta\sigma}{t_f M_f}. \quad (6)$$

2.2. A conventional microstructure having a single bimorph region

Analytical models for microstructures that have a single bimorph region can be derived using a simple moment–curvature relationship from beam theory, assuming that the structural layer and the coating layer are linear elastic materials, and the overall structural deflection is small. We also consider only induced bending effects and neglect axial forces due to stretching effects. These assumptions will be used in deriving analytical models for FOB microstructures later on.

Figure 4 shows the moment, slope and vertical deflection diagrams for a conventional microstructure under a fixed-guided boundary condition. The bimorph region is located on the right-hand side of the structure from ξ to L. $(EI)_1$ and $(EI)_2$ are equivalent stiffnesses of the unimorph region and the bimorph region, respectively. When the overall structure is under various external stimuli, the structure deforms and we

get a flat end or zero slope and finite vertical deflection Δ_A at the guided point A. If we consider force and moment equilibria in the structure, there is no vertical force because of the guided boundary condition at the guided point A. However, there can be a constant induced moment M_A across the structure, which is not determined yet. The relationship between a vertical deflection v and the moment M_A can be expressed as

$$\frac{\mathrm{d}^2 v}{\mathrm{d}x^2} = \frac{M_A}{(EI)_i}, \tag{7}$$

where i is either 1 or 2. On the other hand, for a constant curvature κ of the bimorph section by external stimuli, the second derivative of the vertical deflection can be expressed as

$$\frac{\mathrm{d}^2 v}{\mathrm{d}x^2} = \kappa. \tag{8}$$

Since the slope of the leg θ is equal to $\mathrm{d}v/\mathrm{d}x$, the slope diagram in figure 4 can be drawn from the separate integration of the above two equations (7) and (8). In the slope diagram, the angle θ_{B1} and the angle θ_{B2} are expressed as

$$\begin{aligned} \theta_{B1} &= \frac{M_A}{(EI)_1}\xi + \frac{M_A}{(EI)_2}(L-\xi), \\ \theta_{B2} &= -\kappa(L-\xi), \end{aligned} \tag{9}$$

respectively. Since the net angle θ_B at point B is zero, the magnitudes of θ_{B1} and θ_{B2} should be same. Therefore, from equation (9), the undetermined constant moment M_A can be calculated as

$$M_A = \kappa \cdot \frac{(L-\xi)(EI)_1(EI)_2}{\xi(EI)_2 + (L-\xi)(EI)_1}. \tag{10}$$

If we note that the deflection at the point B is zero, the vertical deflection diagram can be constructed from the integration of the slope diagram as shown in figure 4(*c*). The vertical deflection Δ_A at the point A can be calculated as

$$\begin{aligned} \Delta_A &= \frac{1}{2}\xi^2\frac{M_A}{(EI)_1} + \frac{1}{2}(L-\xi)\frac{M_A}{(EI)_1}\xi \\ &= \frac{1}{2}\frac{M_A}{(EI)_1}L\xi \\ &= \frac{1}{2}\kappa\frac{L\xi(L-\xi)(EI)_2}{\xi(EI)_2 + (L-\xi)(EI)_1}. \end{aligned} \tag{11}$$

From the above equation, it should be noted that if the coating material completely covers the structure, or $\xi = 0$, then the end-point deflection is zero.

When the thickness parameters t_f and t_s are assumed fixed, for the calculation of an optimum ξ to maximize the vertical deflection Δ_A, we need to calculate the first derivative of the deflection Δ_A with respect to ξ. To make the numerator of the first derivative $\Delta_A{}'$ zero, the following equation should be satisfied:

$$[(EI)_2 - (EI)_1]\xi^2 + 2(EI)_1 L\xi - (EI)_1 L^2 = 0. \tag{12}$$

From the above equation, the optimum value ξ^* can be calculated as

$$\xi^* = \begin{cases} \frac{1}{2}L & \text{if } (EI)_1 \simeq (EI)_2 \\ \frac{1}{\sqrt{(EI)_2/(EI)_1}+1}L & \text{if } (EI)_1 \neq (EI)_2. \end{cases} \tag{13}$$

Also, using the optimum ξ^*, the maximum deflection $\Delta_A{}^{\max}$ can be expressed as

$$\Delta_A{}^{\max} = \begin{cases} \frac{1}{8}\kappa L^2 & \text{if } (EI)_1 \simeq (EI)_2 \\ \frac{1}{2}\kappa\frac{1}{(1+\sqrt{(EI)_1/(EI)_2})^2}L^2 & \text{if } (EI)_1 \neq (EI)_2. \end{cases} \tag{14}$$

When the effective stiffness $(EI)_2$ is approximately the same as $(EI)_1$, or the film coating layer thickness is very thin compared to the substrate structural layer thickness ($t_f \ll t_s$), the optimum length parameter ξ^* is just half of the overall structural length L, which is independent of the amount of external stimuli such as temperature, piezoelectric electrical voltage, concentration and surface stress changes. Also, the maximum deflection $\Delta_A{}^{\max}$ is $1/8\kappa L^2$. In a general case, the effective stiffnesses $(EI)_1$ and $(EI)_2$ are different since the thickness parameters are not comparable to each other. So, we have the varying optimum length parameter ξ^* for different width parameters, b_f and b_s, thickness parameters, t_f and t_s, and material properties, M_f and M_s. If we note that $(EI)_2$ is larger than $(EI)_1$, from equation (13) we can see that the optimum length ξ^* is less than a half of the overall structural length. Also, the maximum deflection in the case of $(EI)_1 \neq (EI)_2$ is larger than that in the case of $(EI)_1 \simeq (EI)_2$.

2.3. A flip-over-bimaterial (FOB) microstructure having two bimorph regions

Figure 5 shows a FOB structure having a fixed-guided boundary condition. The lengths of the two bimorph regions are equal, and there is an unimorph region of length η in the middle of the FOB structure. $(EI)_1$ and $(EI)_2$ are equivalent stiffnesses of the unimorph region and the bimorph region, respectively. When the FOB structure is under various external stimuli, it deforms, resulting in a flat end or zero slope and finite vertical deflection Δ_C at the guided point C. If we consider force and moment equilibria in the structure, there is no vertical force because of the guided boundary condition at the guided point C. However, there can be a constant moment M_C across the leg, which is not determined yet. If we consider the slope change by both the constant moment M_C and the curvature κ of the bimorph region, the slope diagram can be drawn as in figure 5(*b*). The slopes θ_{D1} and θ_{D2} are expressed as

$$\begin{aligned} \theta_{D1} &= \kappa\frac{L-\eta}{2} + \frac{M_C}{(EI)_2}\frac{L-\eta}{2} + \frac{M_C}{(EI)_1}\eta + \frac{M_C}{(EI)_2}\frac{L-\eta}{2} \\ &= \kappa\frac{L-\eta}{2} + \frac{M_C}{(EI)_2}(L-\eta) + \frac{M_C}{(EI)_1}\eta, \end{aligned} \tag{15}$$

$$\theta_{D2} = -\kappa\frac{L-\eta}{2}, \tag{16}$$

respectively. Since the net angle θ_D at the point D is zero, the magnitudes of θ_{D1} and θ_{D2} should be same. Therefore, the following relation should be satisfied:

$$M_C\left\{\frac{L-\eta}{(EI)_2} + \frac{\eta}{(EI)_1}\right\} = 0. \tag{17}$$

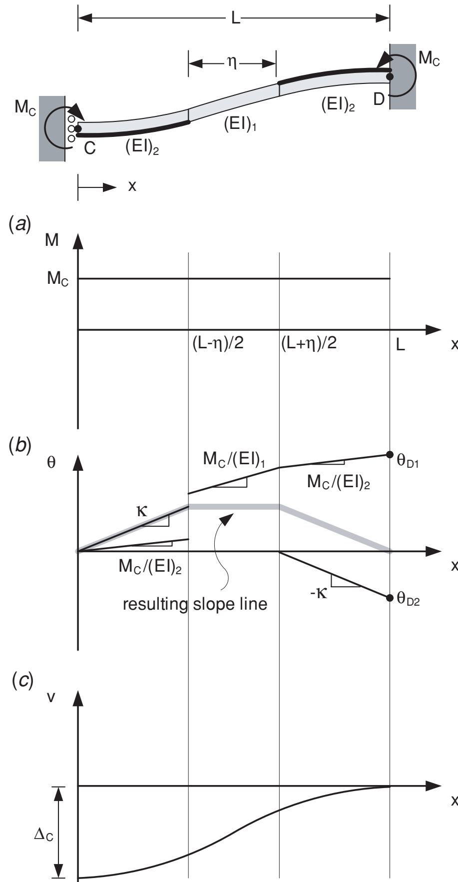

Figure 5. Moment, slope and deflection diagrams of a flip-over bi-material (FOB) microstructure having two bimorph regions under a fixed-guided boundary condition.

If M_C is not zero, the second term of the above equation should be zero. However, since $(EI)_2 \geqslant (EI)_1$, it cannot be satisfied. Therefore, M_C should be zero:

$$M_C = 0. \tag{18}$$

This is an interesting point in the FOB microstructure since the induced bending moment in the conventional microstructure is not zero. Figure 5(*b*) shows the resulting slope line. Also, noting that the deflection at the point D is zero, the vertical deflection diagram can be constructed from the integration of the previous slope diagram, figure 5(*b*). Therefore, the vertical deflection Δ_C at the point C can be calculated as

$$\begin{aligned}\Delta_C &= \frac{1}{2}\kappa\left(\frac{L-\eta}{2}\right)^2 \times 2 + \eta\cdot\frac{L-\eta}{2}\cdot\kappa \\ &= \frac{1}{4}\kappa(L^2-\eta^2).\end{aligned} \tag{19}$$

From the above equation, we can easily see that the optimum length η^* to maximize the vertical deflection Δ_C is zero. When $\eta^* = 0$, the maximum deflection $\Delta_C{}^{\max}$ is

$$\Delta_C{}^{\max} = \tfrac{1}{4}\kappa L^2. \tag{20}$$

3. Model validation

In the conventional microstructure, the end-point deflection thermal sensitivity ($\Delta_A/\Delta T$) varies with the unimorph region

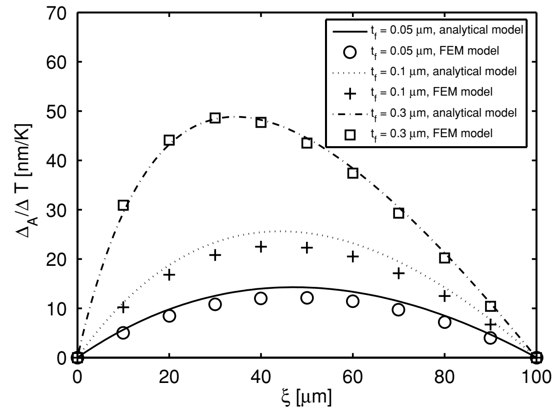

Figure 6. End-point deflection thermal sensitivity of a conventional microstructure ($\Delta_A/\Delta T$) for the unimorph region length ξ ($L = 100\ \mu$m, $b_f = b_s = 5\ \mu$m, $t_s{}^* = 0.5\ \mu$m).

Table 2. Material properties and model parameters used in analytical calculation and FE simulation.

Contents	Au	SiNx
Young's modulus (E) (GPa)	70	100
Thermal expansion coeff. (α) (10^{-6}K^{-1})	14.2	0.8
Poisson's ratio (ν)	0.35	0.27
Density (ρ) (kgm^{-3})	19,300	2,400
Thickness (t) (μm)	Varying	0.5
Leg length (L) (μm)	Varying	100
FE size (μm)	0.5	0.5
FE type	SOLID95	SOLID95

length ξ, as shown in figure 6. Gold and silicon nitride are used as the thin film coating layer and the substrate structural layer, respectively. Commercial FE analysis software, ANSYS, was used and the details of the material and FE model properties are listed in table 2. As shown in figure 6, the derived analytical model predicts well the FEM simulation results for various gold film thickness values t_f. When the thickness of the gold layer increases, as expected by equations (13) and (14), the unimorph region length parameter ξ for the maximum sensitivity shifts to the left position from the center location and the maximum sensitivity to temperature change also increases.

In the FOB microstructure, the end-point deflection thermal sensitivity ($\Delta_C/\Delta T$) varies with the unimorph region length η, as shown in figure 7. Gold and silicon nitride are used as the thin film coating layer and the substrate structural layer, respectively. As shown in figure 7, the derived analytical model predicts well the FEM simulation results for various gold film thickness values t_f. As predicted in the analytical model, the maximum sensitivity can be achieved at $\eta = 0$.

Figure 8 shows a micro-opto-mechanical sensor using interconnected FOB structures. The FOB structure has the feature that one film coating layer (0.2 μm thick gold) is coated on the bottom of the main substrate structural layer (0.5 μm thick silicon nitride) and the other film coating layer (0.2 μm thick gold) is coated on the top of the structural layer. Two symmetric bimorph sensing legs (interconnected FOB structures), which have a fixed-guided boundary condition by anchors and the moving mirror region, are located on

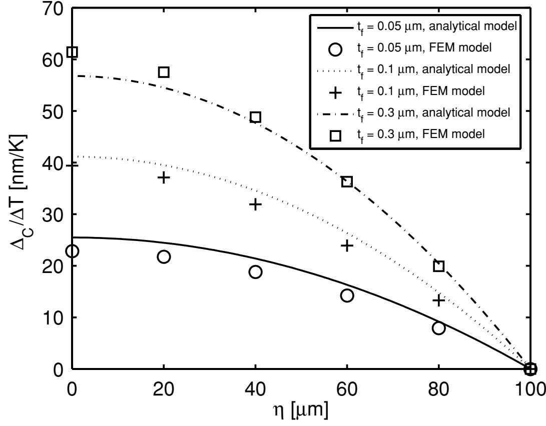

Figure 7. End-point deflection thermal sensitivity of a FOB microstructure ($\Delta_C/\Delta T$) for the unimorph region length η ($L = 100$ μm, $b_f = b_s = 5$ μm, $t_s{}^* = 0.5$ μm).

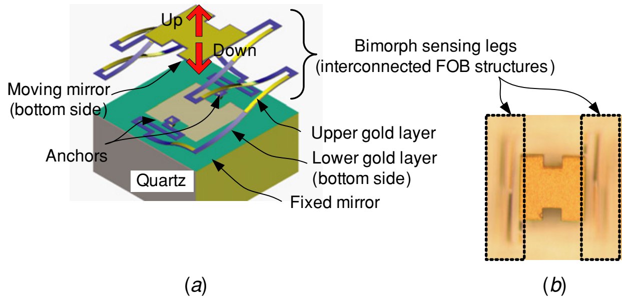

Figure 8. A micro-opto-mechanical sensor using interconnected FOB structures. (*a*) A schematic diagram of the overall sensor design. (*b*) The top view of a fabricated sensor (image focus is on the moving mirror region).

the left and right sides of the moving mirror region. The total deflection of the bimorph sensing legs is converted into a linear displacement of the middle reflecting surface, which is used for optical interferometry between the fixed mirror (on top of the quartz substrate) and the moving mirror (bottom side of the middle structure). The designed sensor was fabricated by surface micromachining techniques using a transparent quartz substrate for optical measurement and a poly-Ge sacrificial layer. For a more detailed fabrication process, refer to [7]. For the fabricated micro-opto-mechanical sensor using interconnected FOB structures, the moving mirror height change was measured for various temperature changes using a commercial white light interferometry setup (VEECO Instruments Inc., Model WYKO NT3300). The measurement results are compared with the calculation results from the analytical model and FE model, as shown in figure 9. The material properties and model parameters given in table 2 were used for the analytical calculation and FE simulation. Since $\eta \approx 0$ in the fabricated sensor, using equation (20) and the superposition principle, the total moving mirror height change can be calculated as

$$\Delta_{\text{mirror}} \approx 1/4 \cdot \kappa_t \left(L_1{}^2 + L_2{}^2 + 2L_3{}^2 + L_4{}^2\right), \tag{21}$$

where κ_t is the curvature induced by thermal strain. Also, L_i ($i = 1$–4), is the length of each FOB beam, which is shown in the inset of figure 9. The thermally induced curvature can be

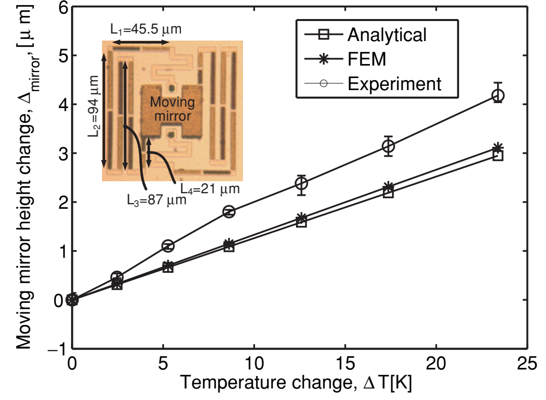

Figure 9. A comparison of moving mirror height change for temperature change.

Table 3. Summary of analytical modeling results.

Contents	Conventional microstructure	FOB microstructure
Induced bending moment	M_A (equation (10))	$M_C = 0$
End-point deflection	Δ_A (equation (11))	Δ_C (equation (19))
Optimum length parameters	ξ^* (equation (13))	$\eta^* = 0$
Maximum deflection	$\Delta_A{}^{\max}$ (equation (14))	$\Delta_C{}^{\max}$ (equation (20))

calculated using equations (2) and (3). As shown in figure 9, the analytical results match the FE simulation results very well. Also, those results agree with the experimental results within about 25%. Discrepancies can be attributed to uncertainties in the material properties of the specimen being tested.

4. Performance analysis

4.1. Sensitivity comparison

The analytical modeling results are summarized in table 3. Using equations (14) and (20), we can calculate the ratio χ of two maximum deflection values for both the conventional and FOB bimorph structures (figure 10):

$$\chi = \frac{\Delta_C{}^{\max}}{\Delta_A{}^{\max}} = \begin{cases} 2 & \text{if } (EI)_1 \simeq (EI)_2 \\ \frac{1}{2}\left(1 + \sqrt{(EI)_1/(EI)_2}\right)^2 & \text{if } (EI)_1 \neq (EI)_2. \end{cases}$$

From the above equation, we can see that when the flexural rigidities of the two regions are approximately same, the FOB structure has up to two times higher deflection for external stimuli such as temperature, concentration and surface stress changes, as compared to the conventional bimorph structure. Furthermore, it should be noted that the FOB structure can generate up to two times higher actuation force, since having the approximately same structural stiffness it can generate up to two times higher deflection than the conventional bimorph structure.

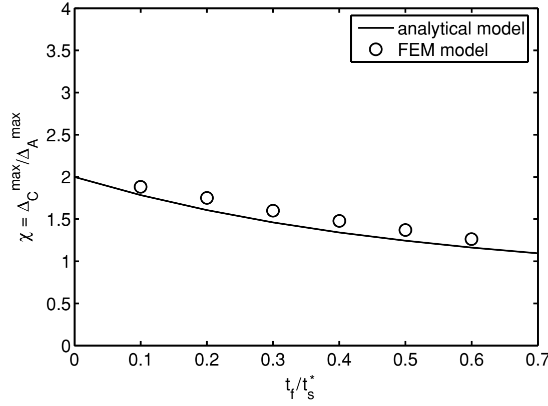

Figure 10. Maximum deflection ratio $\chi = \Delta_C{}^{max}/\Delta_A{}^{max}$ versus thickness ratio $t_f/t_s{}^*$ ($t_s{}^* = 0.5\ \mu$m).

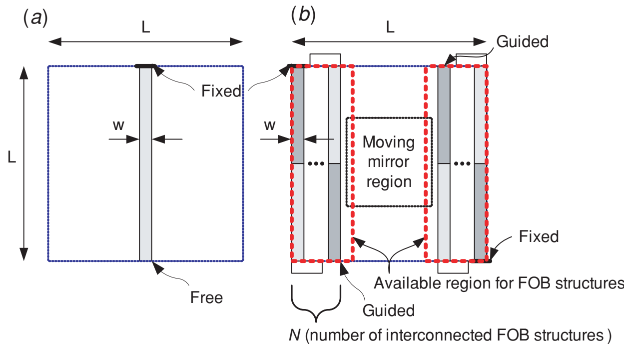

Figure 11. Two device configurations (within the same device footprint, $L \times L$) for a signal-to-noise ratio comparison. (*a*) A simple cantilever structure having length L and width w. (*b*) A device having N interconnected FOB structures. Each FOB structure has length L and width w. The number of interconnected FOB structures N is limited by the available region for FOB structures.

4.2. Signal-to-noise ratio comparison

In this section, the signal-to-noise ratio of a device based on the FOB structure is compared to that of a device based on a conventional cantilever structure, when both devices are confined to the same region $L \times L$, as shown in figure 11. In the noise analysis, we consider an optical measurement as the sensing method, and the three major noise sources (thermal vibration noise, chip substrate temperature stability noise and optical detection noise) are considered.

First, the thermal vibration noise is the fundamental noise limit given by thermal energy $k_B T$, where k_B is the Boltzmann constant, 1.38×10^{-23} J K^{-1} and T is the temperature (300 K). It can be defined as follows:

$$h_n = \sqrt{\frac{2k_B T B}{k\pi f_o Q}}, \tag{22}$$

where B is the measurement bandwidth, which is typically about 30 Hz in CCD detectors [2], k is the spring constant of a structure, f_o is the resonance frequency and Q is the quality factor, which is about 10 at the atmospheric pressure. For the same flexural rigidity EI, the spring constant of a simple cantilever k_{CANT} and that of a FOB design k_{FOB} can be respectively expressed as

$$k_{CANT} = \frac{3EI}{L^3}, \qquad k_{FOB} = \frac{12EI}{L^3} \times \frac{1}{N}, \tag{23}$$

where N is the number of interconnected FOB structures. The resonance frequency of a simple cantilever $(f_o)_{CANT}$ and that of a FOB structure $(f_o)_{FOB}$ can be respectively expressed as

$$(f_o)_{CANT} = \frac{1}{2\pi}\sqrt{\frac{k_{CANT}}{\rho V_{CANT}}}, \qquad (f_o)_{FOB} = \frac{1}{2\pi}\sqrt{\frac{k_{FOB}}{\rho N V_{CANT}}}, \tag{24}$$

where V_{CANT} and ρ are the volume of a simple cantilever structure and density of the structure, respectively. The thermal noise of the FOB design $(h_n^{th})_{FOB}$ and that of the cantilever design $(h_n^{th})_{CANT}$ can be calculated from equations (22)–(24).

Second, the substrate temperature stability noise is a function of the temperature stability limit of the chip temperature control system ΔT_n^{st}, which can be up to 200 μK [17]. The substrate temperature stability noise of the FOB design $(h_n^{st})_{FOB}$ and that of the cantilever design $(h_n^{st})_{CANT}$ can be respectively calculated as follows:

$$(h_n^{st})_{FOB} = \tfrac{1}{4}\kappa_t{}^{st}L^2 \times N, \qquad (h_n^{st})_{CANT} = \tfrac{1}{2}\kappa_t{}^{st}L^2, \tag{25}$$

where κ_t^{st} is the thermally induced curvature by ΔT_n^{st}, which can be calculated using equations (2) and (3).

Third, the optical detection noise is due to limitations in the sensitivity of the optical detection system like a CCD detector, which is used for simultaneous measurements in a two-dimensional sensor array [2], [18]. The interferometric technique is better suited for the FOB design as shown in figure 8. In the case of the cantilever design, the optical lever method can be used [18]. The optical detection noise of the FOB sensor design $(h_n^{opt})_{FOB}$ can be calculated as follows:

$$(h_n^{opt})_{FOB} = (\Delta I/I)/\beta, \tag{26}$$

where $\Delta I/I$ is the CCD detection noise, which is about 3×10^{-4}, and β is the optomechanical sensitivity, which is about 16.1 μm^{-1} [2]. On the other hand, the optical detection noise of the cantilever sensor design $(h_n^{opt})_{CANT}$ can be calculated as follows:

$$(h_n^{opt})_{CANT} = \tfrac{1}{2}\kappa_t{}^{opt}L^2, \tag{27}$$

where $\kappa_t{}^{opt}$ is the curvature induced by the optical noise equivalent temperature $\Delta T_n{}^{opt} = 0.07$ pixel/5 pixel/K $=$ 14 mK [19].

Finally, the total noise of each design can be calculated as follows:

$$(h_n^{tot})_i = \sqrt{(h_n^{th})_i^2 + (h_n^{st})_i^2 + (h_n^{opt})_i^2}, \tag{28}$$

where the subscript i is either FOB or CANT.

On the other hand, the deflection of a simple cantilever h_{CANT} can be expressed as

$$h_{CANT} = \tfrac{1}{2}\kappa L^2, \tag{29}$$

where κ is the induced curvature given by equation (2). As explained in the previous section, the curvature can be generated by several sources such as temperature, electrical voltage, chemical concentration and surface stress changes (table 1). Also, using equation (20) and the superposition

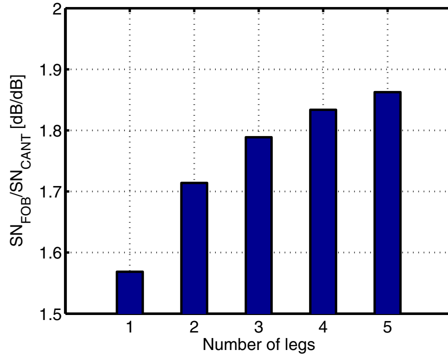

Figure 12. Ratio of SN between FOB and cantilever design, $SN_{\text{FOB}}/SN_{\text{CANT}}$.

Table 4. Estimated noise and signal data comparison for $N = 3$.

Contents	Cantilever design	FOB design
Thermal vibration noise, $h_n{}^{\text{th}}$ (nm)	0.004	0.004
Substrate temperature stability noise, $h_n{}^{\text{st}}$ (nm)	0.007	0.010
Optical detection noise, $h_n{}^{\text{opt}}$ (nm)	0.467	0.019
Total noise, $h_n{}^{\text{tot}}$ (nm)	0.467	0.021
Deflection signal, h (nm)	38.5	57.7
SN	38.3	68.8

principle, the deflection of the FOB design having N serpentine interconnections can be expressed as

$$h_{\text{FOB}} = \tfrac{1}{4}\kappa L^2 \times N. \tag{30}$$

If we define the signal-to-noise ratio SN as

$$SN_i \triangleq 20 \log_{10} \frac{h_i}{\left(h_n{}^{\text{tot}}\right)_i}, \tag{31}$$

where the subscript i is either FOB or CANT, then the signal-to-noise ratio of the FOB design SN_{FOB} and the signal-to-noise ratio between the FOB design and the cantilever design $SN_{\text{FOB}}/SN_{\text{CANT}}$ can be calculated.

Under the surface stress change $\Delta\sigma = 50$ mJ m^{-2}, or its equivalent temperature change $\Delta T = 1.15$ K (calculated from equations (3) and (6)), the signal-to-noise ratio results are shown in figure 12. The material properties are given in table 2. The thicknesses of a gold film coating layer and silicon nitride structural layer are 30 nm and 0.5 μm, respectively. Also, a 5 μm width and a 100 μm length for the cantilever and FOB structures were used. As shown in figure 12, $SN_{\text{FOB}}/SN_{\text{CANT}}$ increases as the number of legs N increases. However, the number of legs N is limited since FOB structures can be placed only on the available dotted region in figure 11(*b*). Table 4 shows the estimated noise and signal data when the allowable number of legs N is equal to 3. It is seen that the signal-to-noise ratio of the FOB design is higher than that of the cantilever design. Its higher signal-to-noise ratio comes from a lower optical detection noise and a higher deflection signal.

5. Conclusions

In this paper we discussed the modeling and performance analysis of two types of micromechanical structures that exhibit the piston-like out-of-plane motion: a conventional microstructure, which has a single bimorph region, and a FOB microstructure, which has two bimorph regions. For both structures, simple analytical expressions for their end-point deflections have been established to facilitate parametric studies of sensor or actuator designs based on these structures. Closed form solutions for the optimum parameters that maximize the end-point deflection of both structures were derived. The induced bending moment of the FOB structure was shown to be zero due to its own symmetric structure. For both microstructures, the derived analytical predictions are in good agreement with those made using FE models. Also, for a fabricated micro-opto-mechanical sensor using interconnected FOB microstructures, these analytical and FE predictions are in reasonable agreement with experimental results. It was found that the developed analytical models are very useful for the parametric study of each structural deflection. The analytically derived deflection expressions and the FE models predict that the FOB microstructures are capable of achieving up to two times higher deflection than a conventional microstructure that has a single bimorph region. Furthermore, for the same device footprint, a sensor design based on the use of interconnected FOB structures has higher signal-to-noise ratio than a simple bimorph cantilever design.

Although the FOB design has been successfully fabricated and demonstrated, and it has been shown to exhibit a superior sensitivity and signal-to-noise ratio, its fabrication is more complex because of the additional bimorph region formation. Therefore, a trade-off exists between the attainable performance enhancements that can be achieved by these devices and their increased fabrication complexity. Through the developed analytical model, parametric study and performance analysis can be performed for the two types of piston-like out-of-plane motion microstructures. These results will be very useful to predict the device performance as well as optimize design parameters. The developed analytical model for bimorph piston-like out-of-plane motion structures can be extended to multimorph piston-like out-of-plane motion structures since the equivalent flexural rigidity and the induced curvature of the multimorph structure can be easily calculated and incorporated in the already developed model.

References

[1] Thundat T and Majumdar A 2003 *Microcantilevers for physical, chemical, and biological sensing: Sensors and Sensing in Biology and Engineering* (Berlin: Springer)

[2] Zhao Y, Mao M, Horowitz R, Majumdar A, Varesi J, Norton P and Kitching J 2002 Optomechanical uncooled infrared imaging system: design, microfabrication, and performance *J. Microelectromech. Syst.* **11** 136–46

[3] Fritz J, Baller M K, Lang H P, Rothuizen H, Vettiger P, Meyer E, Guntherodt H-J, Gerber C and Gimzewski J K 2000 Translating biomolecular recognition into nanomechanics *Science* **288** 316–18

[4] Wu G, Datar R H, Hansen K M, Thundat T, Cote R J and Majumdar A 2001 Bioassay of prostate-specific antigen (PSA) using microcantilevers *Nat. Biotechnol.* **19** 856–60

[5] Hu Z, Thundat T and Warmack R J 2001 Investigation of adsorption and absorption-induced stresses using microcantilever sensors *J. Appl. Phys.* **90** 427–31

[6] Pinnaduwage L A, Boiadjiev V, Hawk J E and Thundat T 2003 Sensitive detection of plastic explosives with self-assembled monolayer-coated microcantilevers *Appl. Phys. Lett.* **83** 1471–73
[7] Lim S-H, Choi J, Horowitz R and Majumdar A 2005 Design and fabrication of a novel bimorph micro-opto-mechanical sensor *J. Microelectromech. Syst.* **14** 683–90
[8] Huang C, Lin Y Y and Tang T A 2004 Study on the tip-deflection of a piezoelectric bimorph cantilever in the static state *J. Micromech. Microeng.* **14** 530–4
[9] Zine-El-Abidine I, Okoniewski M and McRory J G 2005 Tunable radio frequency MEMS inductors with thermal bimorph actuators *J. Micromech. Microeng.* **15** 2063–8
[10] Tuantranont A, Liew L A, Bright V M, Zhang W and Lee Y C 2001 Phase-only micromirror array fabricated by standard CMOS process *Sensors Actuators* A **89** 124–34
[11] Yee Y, Nam H-J, Lee S-H, Bu J U and Lee J-W 2001 PZT actuated micromirror for fine-tracking mechanism of high-density optical data storage *Sensors Actuators* A **89** 166–73
[12] Yang J P, Deng X C and Chong T C 2005 An electro-thermal bimorph-based microactuator for precise track-positioning of optical disk drives *J. Micromech. Microeng.* **15** 958–65
[13] Chu W H, Mehregany M and Mullen R L 1993 Analysis of tip deflection and force of a bimetallic cantilever microactuator *J. Micromech. Microeng.* **3** 4–7
[14] Miyatani T and Fujihira M 1997 Calibration of surface stress measurementswith atomic force microscopy *J. Appl. Phys.* **81** 7099–115
[15] Young W C and Budynas R G 2001 *Roark's Formulas for Stress and Strain* (New York: McGraw-Hill)
[16] Freund L B, Floro J A and Chason E 1999 Extensions of the Stoney formula for substrate curvature to configurations with thin substrates or large deformations *Appl. Phys. Lett.* **74** 1987–9
[17] Choi J, Yamaguchi J, Morales S, Horowitz R, Zhao Y and Majumdar A 2003 Design and control of a thermal stabilizing system for a MEMS optomechanical uncooled infrared imaging camera *Sensors Actuators* A **104** 132–42
[18] Yue M, Lin H, Dedrick D E, Satyanarayana S, Majumdar A, Bedekar A S, Jenkins J W and Sundaram S 2004 A 2-D microcantilever array for Multiplexed biomolecular analysis *J. Microelectromech. Syst.* **13** 290–99
[19] Yue M 2004 Multiplexed label-free bioassays based on nanomechanics and nanofluidics *PhD dissertation* University of California, Berkeley